Effect of competing mechanisms on fracture toughness of metals with ductile grain structures

Yan Li[a,*], Min Zhou[b]

[a] Department of Mechanical and Aerospace Engineering, California State University, Long Beach, CA 90840, USA
[b] The George W. Woodruff School of Mechanical Engineering, School of Material Science and Engineering, Georgia Institute of Technology, Atlanta, GA 30332-0405, USA

ABSTRACT

The fracture toughness of ductile materials depends on the combined effect of plastic dissipation in the constituents and energy spent on creating new crack surfaces. The design of polycrystalline metals with improved fracture toughness requires in-depth understanding of two levels of competing mechanisms: the competition between plastic deformation and crack formation as well as the competition between transgranular and intergranular fracture. Currently, no systematic approach exists to analyze the effects of the two competitions. The fundamental challenges lie in the difficulty in separating the two forms of energy dissipation and inadequate knowledge about the correlation between fracture mechanisms and material fracture toughness. In this paper, a multiscale framework based on the Cohesive Finite Element Method (CFEM) is developed to quantify the two levels of competitions and to predict the fracture toughness of ductile materials by calculating the *J*-integral at the macroscale. The fracture surface energy for the crack paths associated with different types of failure mechanisms is evaluated through explicit simulation of crack propagation at the microstructure level. The calculations carried out here concern the AZ31 Mg alloy, but the overall approach applies to other materials as well. Results indicate that a proper balance between transgranular and intergranular failure can lead to optimized fracture toughness. Microstructures with refined grain sizes and balanced bonding strength in grains and grain boundaries can best promote the manifestation of favorable failure mechanisms, and as a result, enhance fracture toughness.

1. Introduction

From the energy point of view, a crack can grow only when the energy available at the crack tip is sufficient to balance out the energy required for crack propagation. Therefore, a key aspect of designing high toughness materials is to promote favorable failure mechanisms which can lead to maximized energy dissipation. For brittle materials, the most effective way to improve fracture toughness is to create tortuous crack paths since, in the absence of plasticity, the total energy released is transformed into surface energy alone. This can be achieved by, for example, introducing refined second-phase reinforcements, appropriately balanced interphase bonding strength and interface stiffness, and through grain bridging [1–5]. For ductile materials, the fracture resistance depends on the sum of energy spent on both surface generation and bulk plastic deformation. Osovski et al. [6] studied the effect of loading rate on ductile fracture toughness. They found that the total plastic dissipation and the plastic dissipation associated with the

---

ductile fracture process increase with increasing strain rate. Srivastava et. al [7] also found that void density determines void growth and coalescence and in turn influences ductile fracture toughness by creating different crack trajectories. In polycrystalline metals, intergranular fracture usually leads to tortuous crack paths via crack propagation along grain boundaries. While surface energy dissipation is enhanced, this form of fracture may discourage energy dissipation through plastic deformation in the grains and, therefore, may not always lead to higher fracture resistance [8]. The grain boundary induced embrittlement which leads to inter-granular fracture has been discussed by many researchers. For example, Prakash et al studied the influence of grain boundary strength on microstructure dependent crack propagation [9]. Watanabe and Tsurekawa [10] provided insights on solving inter-granular brittleness through grain boundary engineering. Transgranular fracture, on the other hand, leads to smaller total areas of fracture surfaces but allows more significant plastic energy dissipation to occur and, therefore, leads to overall more ductile material response [11]. The interplay between bulk plastic deformation and the fracture mechanism being activated during the failure process has not been systematically studied, much less quantified. It is not clear how to control the two forms of energy dissipation so as to maximize the total energy release. The design of polycrystalline metals with improved fracture toughness requires elucidation of the two levels of competition by considering the effects of microstructure, one being the competition between bulk material deformation and crack formation, and the other being the competition between transgranular fracture and intergranular fracture.

The biggest challenge in quantifying the above competitions is to correlate each mechanism with the material's fracture toughness. Experimentally and numerically, a number of measures, including the crack-tip opening displacement (CTOD), the crack-tip opening angle (CTOA) and the *J*-integral, have been widely used to evaluate the fracture toughness of ductile materials [12–14]. However, these approaches do not attempt to address the competing mechanisms which are activated during the failure process. The reason is several-fold. First, these measurements cannot separate the contributions of different mechanisms, such as crack surface creation vs. plastic deformation or different types of crack faces/fracture sites. It is not clear which contribution is more important for material toughening or how much each mechanism contributes to the overall energy dissipation, CTOD or CTOA. Besides, these measurements only evaluate material fracture toughness at the macroscale. Fundamentally, it is not possible to resolve each type of fracture mechanism associated with the crack propagation process without considering microstructure information.

Here, a multiscale computational framework is developed to quantify the two levels of competitions by accounting for micro-scopic heterogeneity and hierarchy. This framework allows representation of realistic microstructures and account of microstructural level of deformation, damage and failure mechanisms. The *J*-integral is employed to evaluate the fracture toughness while all the microscopic information and relevant process are considered. The cohesive finite element method (CFEM) is used to track the crack propagation at the microstructure level. To explicitly resolve transgranular and intergranular fracture, cohesive surfaces are embedded along the edges of all bulk elements in the microstructure region [15–19]. The constitutive relations for the bulk grains and cohesive surfaces within the grains and along the grain boundaries are specified separately. The part of the energy dissipation rate associated with surface formation can be evaluated directly by measuring the corresponding crack length. The part of the energy dissipation rate associated with bulk plastic dissipation is obtained as the difference between the calculated *J* during crack growth and the surface energy dissipation rate.

This framework provides physical insight on the influence of competing mechanisms on the fracture toughness of polycrystalline metals. The methodology is useful for both the selection of materials and the tailoring of microstructure to improve material fracture resistance and reliability. Although calculations in this paper only focus on AZ31 Mg alloy, the framework developed here can be applied to other polycrystalline metals.

2. CFEM–based multiscale framework

An edge-cracked specimen under Mode I tensile loading is modeled as shown in Fig. 1. This model consists of two length scales. The microstructure region has a width of 0.125 mm, a length of 0.25 mm and a pre-crack length of 0.18 mm. The entire square specimen has a side length of 0.45 mm. A boundary velocity of v = 5 mm/s is imposed at the top and bottom edges of the specimen to effect symmetric Mode I tensile loading. The remaining edges of the specimen are traction-free. Conditions of plane strain are assumed to prevail.

An elasto-plastic, isotropic constitutive relation is assumed for the bulk constituents which only exist in grains. Specifically, all the grains follow J2 plasticity without hardening. Young's modulus $E = 45$ GPa and Poisson's ratio $\nu = 0.35$ are employed according to Guo et al. [20,21]. Calculations carried out consider yields stress σ_y varying from 100 MPa to 575 MPa. The effect of yield stress on fracture toughness and failure mechanisms will be discussed in detail in Section 4.1. Although a simple constitutive model is used here, the overall framework allows the competitions between different fracture mechanisms outlined above and microstructure effects on fracture toughness to be analyzed. A more involved constitutive model such as a crystalline plasticity model, though more realistic and considers more factors, would also complicate an initial study aimed at developing an approach for relating micro-structure to macroscopic fracture toughness because of its large number of parameters. Ultimately, of course, a more comprehensive model is needed to predict the fracture toughness of real engineering materials.

Cohesive elements are embedded only in the microstructure region so as to resolve arbitrary crack paths. The cohesive elements along both grain boundaries and within grains follow the bilinear traction-separation law shown in Fig. 2. This is an idealization that can be easily modified to accommodate more detailed and quantitative information regarding, for example, the lower cohesive strength or separation energy of intergranular versus transgranular propagation. This law is derived from a potential Φ which is a function of the separation vector $\mathbf{\Delta}$ through a state variable defined as $\lambda = \sqrt{(\Delta_n/\Delta_{nc})^2 + (\Delta_t/\Delta_{tc})^2}$. This variable describes the effective instantaneous state of mixed-mode separations. Here, $\Delta_n = \mathbf{n}\cdot\Delta$ and $\Delta_t = \mathbf{t}\cdot\Delta$ denote, respectively, the normal and tangential
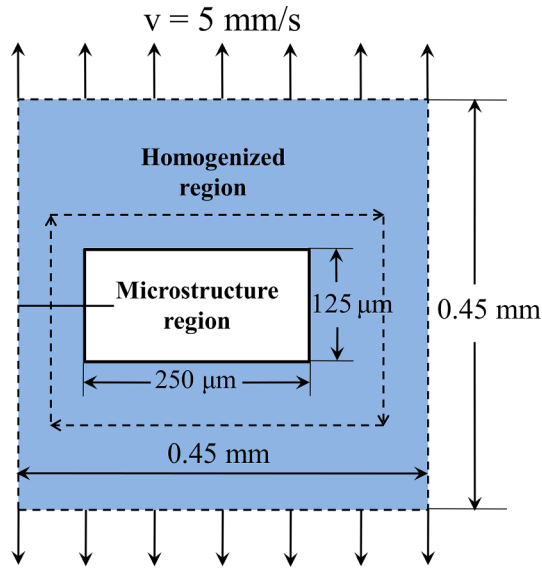
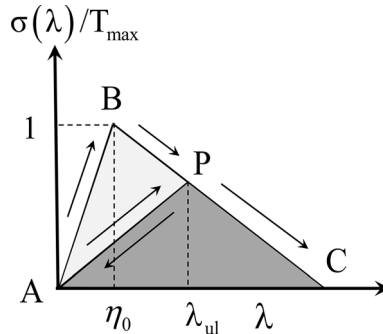**Fig. 1.** Specimen configuration under Mode-I loading.

Fig. 2. Scheme of traction-separation law used in the analysis.

components of Δ, with $\boldsymbol{n}$ and $\boldsymbol{t}$ being unit normal and tangent vectors. Δ_{nc} is the critical normal separation at which the cohesive strength of an interface vanishes under conditions of pure normal deformation ($\Delta_t = 0$). Similarly, Δ_{tc} is the critical tangential separation at which the cohesive strength of an interface vanishes under conditions of pure shear deformation ($\Delta_n = 0$). $T_{\max}$ represents the maximum traction that the cohesive element can sustain at the onset of irreversible separation.

In order to account for the irreversibility of separations, a parameter $\eta = \max\{\eta_0, \ \lambda_{ul}\}$ is defined. As illustrated in Fig. 2, η_0 is the initial value of η which defines the stiffness of the original undamaged cohesive surface, while λ_{ul} is the hitherto maximum value of λ at which an unloading process was initiated. It should be noted that λ_{ul} is associated with the onset of an unloading event and is not necessarily the hitherto maximum value of λ. λ_{ul} represents the current (reduced) stiffness of the cohesive surfaces after damage and unloading have occurred. Furthermore, η_0 represents the characteristic value of effective separation λ at which the effective traction σ for a cohesive surface pair reaches the strength reaches the strength $T_{\max}$ of the undamaged surface. λ_{ul} stands for the critical level of λ at which σ reaches the reduced strength $T_{\max}(1 - \eta)/(1 - \eta_0)$ of the hitherto damaged cohesive surface pair. The specific expression for potential Φ is of the form

$$\Phi = \Phi(\lambda, \eta) = \begin{cases} \Phi_0\left(\frac{1-\eta}{1-\eta_0}\right)\left(\frac{\lambda^2}{\eta}\right), & \text{if } 0 \leqslant \lambda \leqslant \eta, \\ \Phi_0\left(\frac{1-\eta}{1-\eta_0}\right)\left(1 - \frac{(1-\lambda)^2}{1-\eta}\right), & \text{if } \eta \leqslant \lambda \leqslant 1, \\ 0, & \text{if } \lambda > 1. \end{cases} \tag{1}$$

As indicated in Fig. 2, separation occurs elastically and the cohesive energy stored (work done in causing separation) is fully recoverable between A and B ($0 \leqslant \lambda \leqslant \eta_0$), and damage in the form of microcracks and other small-scale defects does not occur. Between B and C ($\eta_0 \leqslant \lambda \leqslant 1$), material degradation causes progressive reduction in the strength of the cohesive surfaces. This represents a phenomenological account of the effects of microcracks and other defects not explicitly modeled in the CFEM model. Unloading from any point P follows path PA and subsequent reloading follows AP and then PC. Part of the work expended on causing
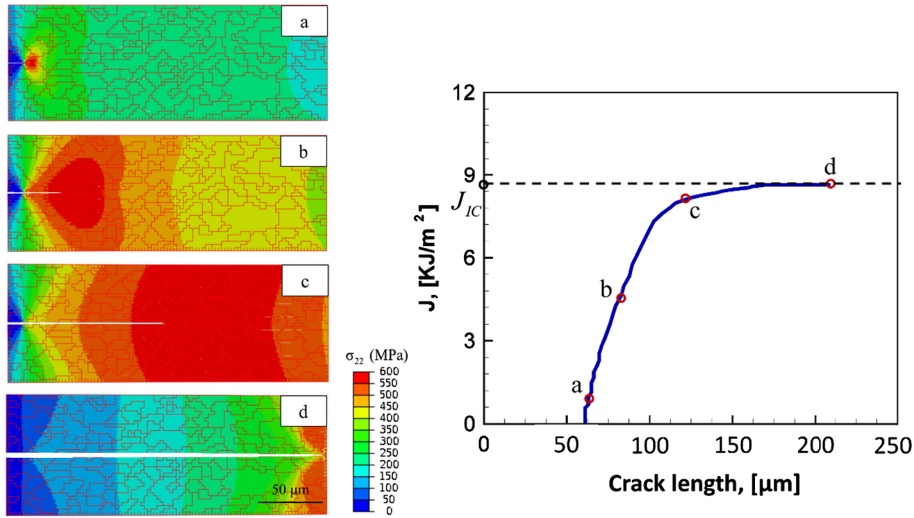
Fig. 3. Crack propagation in an AZ31 Mg microstructure and the evolution of *J* curve during the crack propagation process.

the separation in this regime is irreversible, as indicated by the hysteresis loop ABP which implies dissipation during the softening process. Correspondingly, there is a decrease in the maximum tensile strength of the cohesive surface. This is reflected in the elastic reloading of the interface along AP and further softening along path PC.

3. Semi-analytical model for energy separation in J-integral

3.1. J-integral based fracture toughness evaluation

As illustrated by the dashed lines in Fig. 1, the *J*-integral is calculated along an arbitrary contour within the homogenized region by following

$$J = \int_{\Gamma} \left[\left(\int_0^t \tau : d\mathbf{E} + \frac{1}{2}\rho\dot{\mathbf{u}}\cdot\dot{\mathbf{u}} \right) dx_2 - \mathbf{t}\cdot\frac{\partial \mathbf{u}}{\partial x_1} ds \right] + \int_A \left(\rho\ddot{\mathbf{u}}\cdot\frac{\partial \mathbf{u}}{\partial x_1} - \rho\dot{\mathbf{u}}\cdot\frac{\partial \dot{\mathbf{u}}}{\partial x_1} \right) dA,$$

(2)

where $\mathbf{t}$ is the traction on a surface with normal N in the reference configuration, $\mathbf{u}$, $\dot{\mathbf{u}}$ and $\ddot{\mathbf{u}}$ are the displacement, velocity and acceleration, respectively. $\tau = \det |\mathbf{F}|\ \sigma$ is the Kirchoff stress with $\mathbf{F}$ and σ as deformation gradient and Cauchy stress, respectively. $\mathbf{E}$ represents the Lagrangian strain and $E_{ij} = \frac{1}{2}(F_{ki}F_{kj} - \delta_{ij})$. $\rho = 1738$ kg/m^3 is the mass density.

The evolution of *J* curve for a specific AZ31 Mg microstructure is shown in Fig. 3. To illustrate the fracture process studied, four snap shots are extracted from the crack propagation process and the corresponding *J* values are marked in the *J*-a curve. It is noted that the crack starts to propagate at (a). Subsequently, the *J* value increases significantly until the crack has traversed a sufficiently representative part of the microstructure. The increase of *J* from (c) to (d) is not as pronounced as the increase from (a) to (c). The critical driving force J_{IC}, which is needed to balance out the fracture resistance of the material, is defined at moment (d) when the maximum *J* value is reached. It is worth mentioning that J_{IC} is a preferred parameter for quantifying fracture toughness based on the sample configuration as shown in Fig. 1. K_{IC} cannot be predicted from the following equation

$$K_{IC} = \sqrt{\frac{J_{IC}E}{1 - \nu^2}},$$

(3)

since Small Scale Yielding (SSY) condition is not met. Here E and ν are the Young's modulus and Poisson's ratio, respectively. The Small Scale Yielding (SSY) condition requires that

$$a, b, t > 2.5\left(\frac{K_{IC}}{\sigma_y}\right)^2$$

(4)

with a, b and t representing the pre-crack length, specimen width and thickness, respectively. This condition necessities the use of a very large specimen for most ductile materials, a very demanding condition to meet computationally when microstructure details need to be considered. For example, an AZ31 Mg specimen with $K_{IC} = 250$ MPa$\sqrt{\text{m}}$ and $\sigma_y = 350$ MPa would require a, b, $t > 95.3$ mm according to Somekawa and Mukai [22]. The specimen width $b = 0.45$ mm in this study as shown in Fig. 1 is far below the required 95.3 mm. In fact, few existing experimental studies on AZ31 Mg alloys meet the SSY requirement [22–26]. Instead, *J* value is preferably used to quantify fracture toughness since the *J* dominance criterion only requires
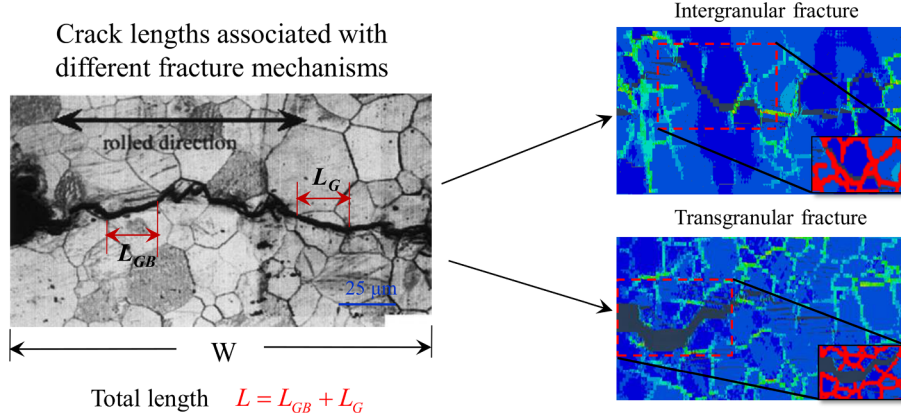
Fig. 4. A schematic illustration of crack trajectory in AZ31 Mg alloy and crack lengths associated with different fracture mechanisms. Left picture reproduced from Somekawa and Mukai's work [22].

$$b > 25\frac{J_{IC}}{\sigma_y}. \tag{5}$$

For AZ31 Mg alloy, J_{IC} is a valid fracture toughness characterization when the specimen width $b > 0.0243$ mm. Therefore, the specimen dimensions employed in Fig. 1 satisfy the J dominance requirement. It can be concluded that J_{IC} is a better measure than K_{IC} for assessing material fracture toughness since the size requirements for J testing are much less severe than for K testing.

This specimen design allows the calculations to approximate conditions of quasi-static loading with high computational efficiency. It is found that the change of J is negligible as the crack speed spans one to two orders of magnitude. It is expected since the constitutive relations assumed here is rate-independent.

3.2. Contributions to J-integral

A crack path in AZ31 Mg alloy can include both transgranular and intergranular fracture as shown by the experimental work of Somekawa and Mukai [22] and our simulations in Fig. 4. As a measure of the material's resistance to fracture, the J value calculated from Eq. (2) includes contributions from both plastic dissipation and the energy spent on creating new surfaces. Specifically, the energy release rate J can be stated as

$$J = \frac{\partial U_f}{\partial A} = J_s + J_p \approx \frac{(\Phi_G L_G + \Phi_{GB} L_{GB})t_t}{W t_t} + \frac{\int_0^t (\int_V \sigma : \dot{\varepsilon}^{pl} dV) dt}{W t_t} = \frac{L}{W}\left(\Phi_G \frac{L_G}{L} + \Phi_{GB} \frac{L_{GB}}{L}\right) + \frac{\int_0^t (\int_V \sigma : \dot{\varepsilon}^{pl} dV) dt}{W t_t}$$

$$= \xi\left(\frac{T^G_{max}}{\sigma_y}, \frac{T^{GB}_{max}}{\sigma_y}\right)(\Phi_G H_G + \Phi_{GB} H_{GB}) + \frac{\int_0^t (\int_V \sigma : \dot{\varepsilon}^{pl} dV) dt}{W t_t}, \tag{6}$$

where J_p and J_s denote the energy release rate associated with plastic dissipation and surface formation, respectively. U_f is the total energy released over the projected crack length W. $A = W t_t$ is the total projected crack surface area with t_t being the specimen thickness. It should be noted that W is the projected crack length in the direction of crack propagation, while L is the total crack length. Specifically, $L = L_G + L_{GB}$, with L_G and L_{GB} representing the crack arc lengths within the grains and along the grain boundaries, respectively. Accordingly, H_G and H_{GB} are the proportions of crack lengths associated with transgranular and intergranular fracture, respectively. Both H_G and H_{GB} can be explicitly extracted from the CFEM simulations. Φ_G and Φ_{GB} are, respectively, the fracture energies within the grains and along the grain boundaries as defined in Eq. (1). ξ measures the ratios between the actual crack length L and the projected crack length W. It captures the influences of microstructural attributes on the crack tortuosity. Here, ξ is defined as the crack length multiplication factor (CLMF). As discussed in the following section, ξ primarily depends on the cohesive bonding strength within the grains (T^G_{max}), the cohesive bonding strength along the grain boundaries (T^{GB}_{max}), and the yield stress of grains σ_y.

The model and the approach taken here allow J to be calculated as a function of microstructure and J_s to be quantified by explicitly tracking the crack propagation. Specifically, $J_p = J - J_s$ is calculated during the course of crack initiation and propagation.

4. Results and discussion

Four sets of calculations are conducted to systematically analyze the effect of yield stress, cohesive strength of the grains/grain boundaries and microstructure morphology on the activation of failure mechanisms and their respective individual effect on the overall fracture resistance. The microstructures in Fig. 5 are employed. These microstructures include the actual AZ31 Mg microstructure [27] which is used to study the effect of yield stress, effect of cohesive strength of the grains/grain boundaries (see Sections 4.1–4.3) and effect of microstructure morphology. In addition to these actual microstructures, three microstructures generated using
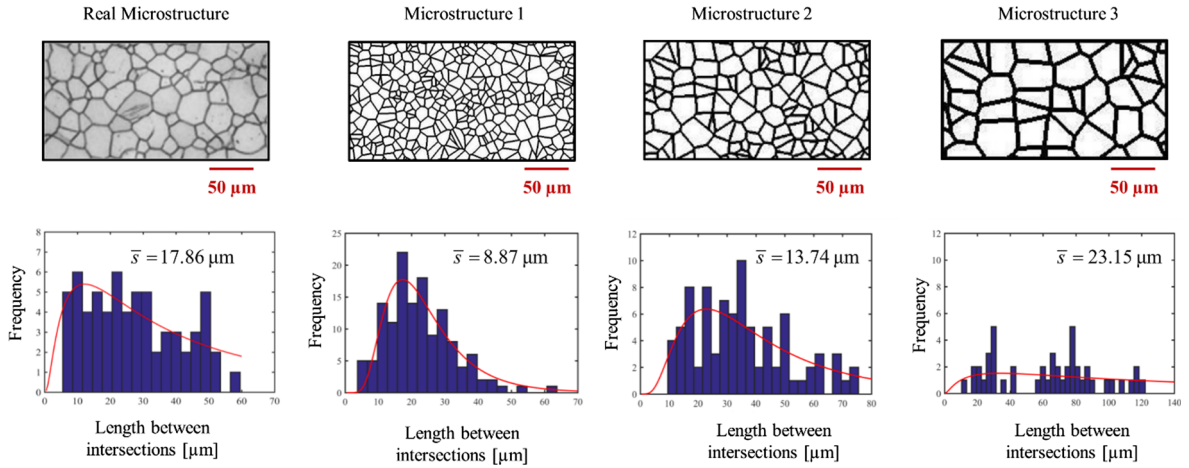
Fig. 5. List of microstructures employed in the calculations and comparison of distribution of length between intersections.

Table 1
Summary of test line – grain boundary intersections and average grain sizes for the four microstructures in Fig. 7.

Intersections	Real microstructure	Microstructure 1	Microstructure 2	Microstructure 3
Line 1	15	28	18	12
Line 2	15	27	17	13
Line 3	10	31	17	11
Line 4	14	24	20	9
Line 5	16	31	19	9
Average grain size $\bar{s}$ (µm)	17.86	8.87	13.74	23.15

the Voronoi tessellation [28] are used to study the effect of microstructure morphology (see Section 4.4). To obtain a characterization of the microstructures in the context of the fracture analysis, we use the average grain interception (AGI) method to evaluate the grain size [29]. Five random straight lines are drawn through each microstructure in the horizontal direction. The number of grain boundaries intersecting each line is counted. Table 1 summaries the number of intersections along each line for the four microstructures. The average grain size $\bar{s}$ is calculated by dividing the actual line lengths by the number of intersections. The distributions of line length between intersections in each microstructure are also plotted in Fig. 5.

4.1. Effect of yield stress

In the first set of calculations, the cohesive elements in grains and along the grain boundaries have the same cohesive properties of $\Phi^G = \Phi^{GB} = 7.5$ kJ/m^2 and $T_{max}^G = T_{max}^{GB} = 350$ MPa. This indicates that transgranular and intergranular fracture are equally likely to occur purely based on bonding and fracture behavior. The only variation considered here is the yield stress of grains. It is assumed that all grains have the same yield stress and the material is homogenous and isotropic. In the following calculations, $\sigma_y = [100, 575]$MPa with an interval of 25 MPa. Therefore, a total of 20 cases are analyzed.

As shown by the J-a (J-crack length) curves in Fig. 6(a), J value initially increases as the crack propagates, but eventually saturates to a certain plateau level. The corresponding J_{IC} under each yield stress is extracted when the maximum J value is reached. Fig. 6(b) shows that increasing the yield stress of the grains leads to lower fracture resistance as measured by J_{IC}.

For all the cases in Fig. 6, the crack tends to go through the grains instead of following the grain boundaries, although the grains and grain boundaries have the same fracture energy. As illustrated in Fig. 7, transgranular fracture is the only failure mode observed. The change of grain yield stress has a negligible effect on the crack path as the total crack length L is equivalent to the projected length W. Therefore, the crack length multiplication factor ξ is 1 for all the cases. Eq. (6) can be further simplified as

$$J = \frac{\partial U_f}{\partial A} = J_s + J_p \approx \Phi_G H_G + J_p. \tag{7}$$

Obviously, the material response is more ductile when the yield stress is lower. As shown in Fig. 8, plastic dissipation becomes more pronounced as the yield stress decreases. Fig. 8 shows that all J_s curves saturate at the same level. The plateau of J_s indicates the maximum attainable surface energy release rate for this type of microstructure configuration is a constant under identical grain and grain boundary properties. The evolutions of J_p and J_s under four representative yield stress levels are shown in Fig. 9. Lower levels of yield stress lead to more intensive plastic dissipation. As the yield stress decreases from 525 MPa to 125 MPa, the initial slope of J_p becomes increasingly steeper. The plateau of J is reached as J_p achieved a steady value. It can be concluded that J_p plays a more important role in material toughening since the improvement of J_s is quite limited when transgranular fracture is the only failure
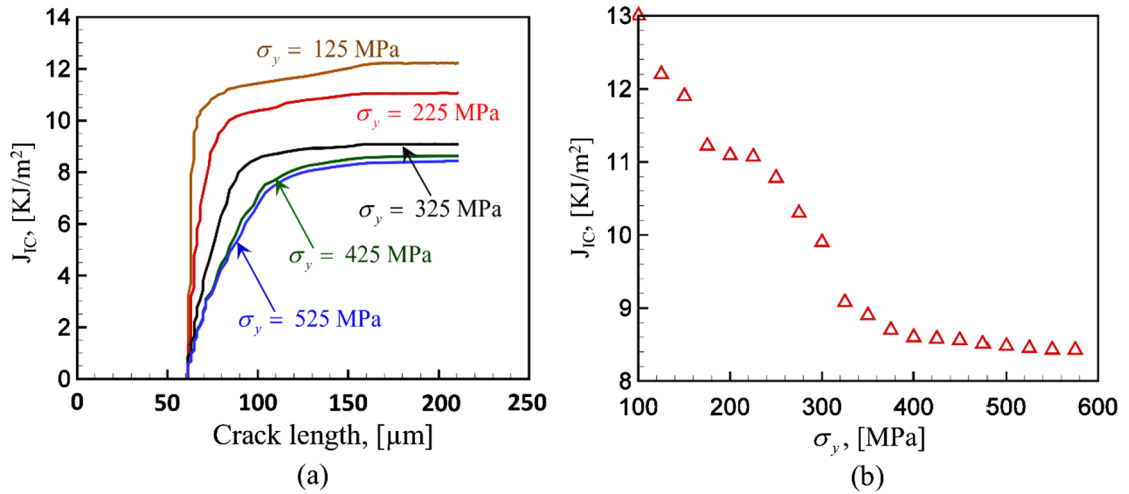
Fig. 6. (a) Evolution of J during the crack propagation, and (b) J_{IC} predicted under different yield stress σ_y.
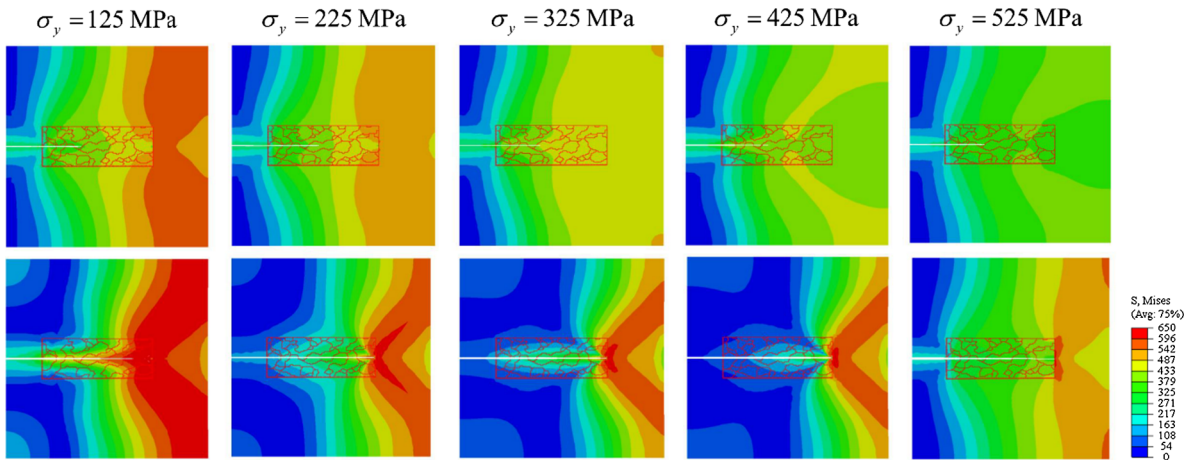

Fig. 7. Transgranular fracture in an isotropic microstructure under differ yield stresses.
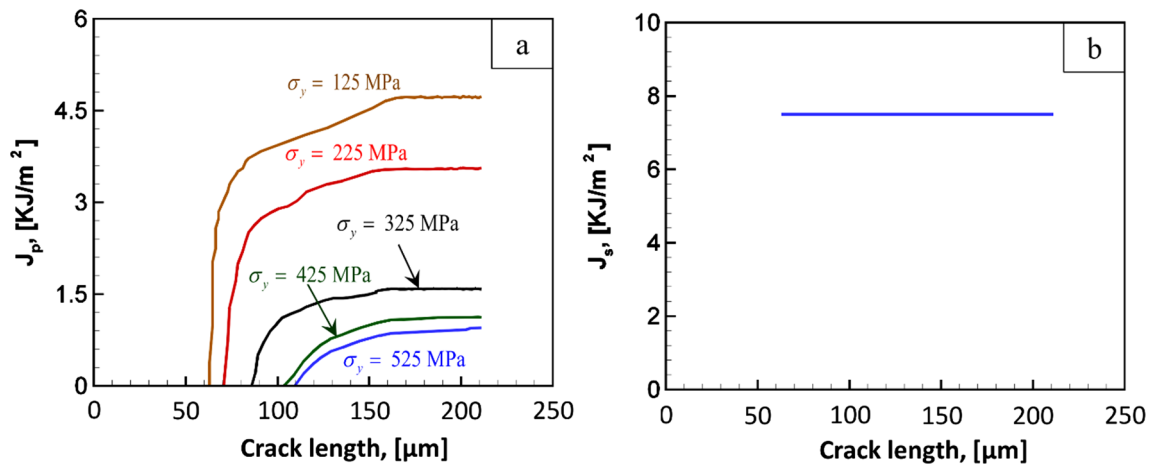

Fig. 8. Separation of J in Fig. 6(a) into energy dissipation in terms of (a) plastic deformation and (b) surface formation.
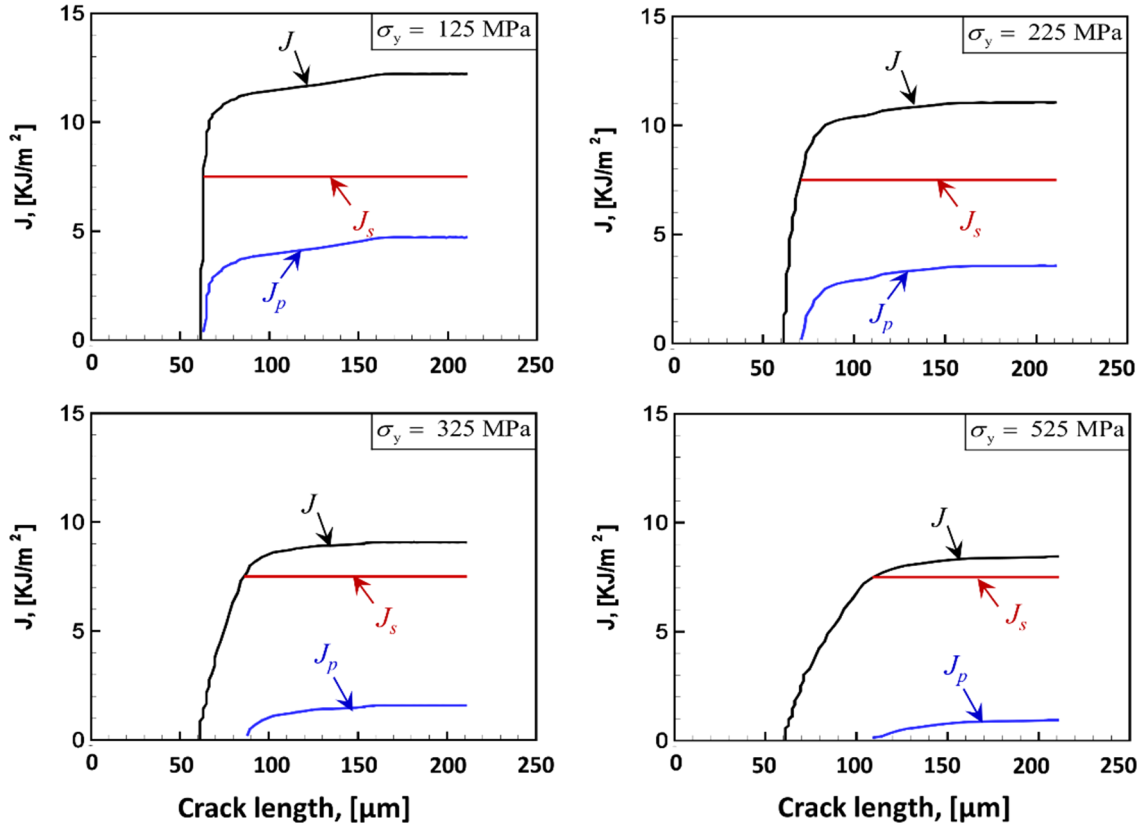
Fig. 9. Separation of J_p and J_s under four representative yield stress levels.

mode observed. This set of calculations serve as the baseline for the following studies when both transgranular and intergranular fractures are present.

4.2. Effect of cohesive strength of grains T^G_{max}

In this set of calculations, all grains have the same yield stress $\sigma_y = 150$ MPa. $\Phi_G = \Phi_{GB} = 7.5$ kJ/m² for both the grains and the grain boundaries. The maximum cohesive strength along the grain boundaries is $\mathrm{T}^{GB}_{max} = 350$ MPa, and the cohesive strength in the grains T^G_{max} is systematically varied from 100 MPa to 575 MPa with an interval of 25 MPa.

As shown in Fig. 10(a), transgranular fracture is the only failure mode observed when $\mathrm{T}^G_{max} = 175$ MPa. As T^G_{max} increases, the crack starts to propagate into the grain boundaries. Intergranular fracture gradually becomes the dominated failure mode. The competition between transgranular fracture and intergranular fracture is quantified in Fig. 10(b). Here, L_G/W and L_{GB}/W represent the proportions of transgranular fracture and intergranular fracture, respectively. L/W, which is the sum of L_G/W and L_{GB}/W, is defined as the crack length multiplication factor ξ as in Eq. (6). As illustrated in Fig. 10(b), $\mathrm{T}^G_{max} \approx 385$ MPa corresponds to the intersection of the curve for L_G/W and curve for L_{GB}/W. This point indicates the transition from transgranular fracture dominance to intergranular fracture dominance. Transgranular fracture is the dominant failure mode when $\mathrm{T}^G_{max} < 385$ MPa as L_G/W is always above L_{GB}/W. The trend reverses when $\mathrm{T}^G_{max} > 385$ MPa as intergranular fracture takes over and becomes the dominated failure mode. The maximum J_{IC} is reached at $\mathrm{T}^G_{max} \approx 425$ MPa rather than at the transition point $\mathrm{T}^G_{max} \approx 385$ MPa. Although $\mathrm{T}^G_{max} \approx 425$ MPa corresponds to the peak of the curve for L/W, the maximization of J_{IC} not only requires the maximization of crack length L but also a combined contribution from both J_s and J_p. When transgranular fracture is the dominated failure mode ($\mathrm{T}^G_{max} = 175$ MPa and $\mathrm{T}^G_{max} = 275$ MPa in Fig. 10(a) and Fig. 11), J_s is approximately a constant and constitutes most of the driving force J. Although J_p keeps increasing at the early stage of crack propagation, it starts to saturate when unsteady crack propagation occurs, leading J to reach the plateau. When $\mathrm{T}^G_{max} > 300$ MPa, the crack tends to propagate into grain boundaries. As T^G_{max} increases, microcracks starts to initiate along the grain boundary in addition to the pre-crack tip. Coalescence of the microcracks along the grain boundaries promotes surface area creation and increased J_s. More importantly, some of the microcracks tends to propagate into the neighboring grains without breaking them. These uncracked grains can serve as "bridges" to allow further deformation and more pronounced plastic energy dissipation. This can be explained from Fig. 11 that J_p goes beyond J_s during the course of crack propagation when $\mathrm{T}^G_{max} = 425$ MPa. Further increase of T^G_{max} can promote intergranuar fracture but suppress plastic deformation since fewer cracks go to the grains. When T^G_{max} increases from 425 MPa to 525 MPa, the improvement of J_s is at the cost of sacrificing J_p. It can be concluded
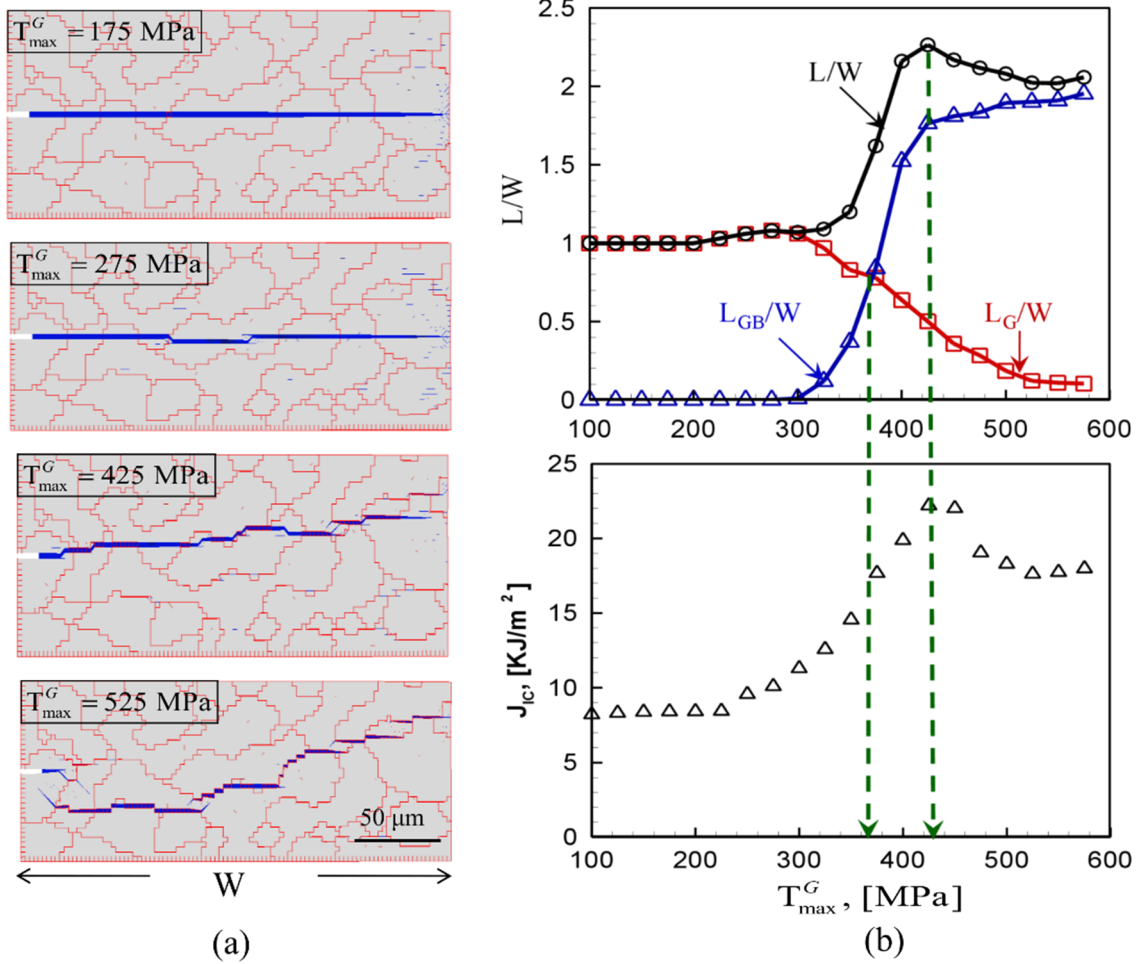
Fig. 10. (a). Crack trajectories under different grain cohesive strength T_{max}^G and (b). illustration of the competition between transgranular and intergranular fracture and its effect on fracture toughness.

that $T_{max}^G \approx 425$ MPa allows this combined transgranular and intergranular fracture with balanced contributions from both J_s and J_p, leading to maximized J_{IC}.

4.3. Effect of cohesive strength of grain boundaries T_{max}^{GB}

Conclusions from the above discussions indicate that $T_{max}^G = 425$ MPa can lead to the highest J_{IC} when T_{max}^{GB} is fixed at 350 MPa. In this set of calculations, T_{max}^{GB} is systematically varied from 100 MPa to 575 MPa with an interval of 25 MPa. T_{max}^{GB}/T_{max}^G considered here spans from 0.24 to 1.35. $\sigma_y = 150$ MPa and $\Phi_G = \Phi_{GB} = 7.5$ kJ/m² for both the grains and the grain boundaries.

According to Figs. 10 and 12, both T_{max}^G and T_{max}^{GB}/T_{max}^G influence the activation of failure mechanisms and, consequently, alter the material fracture resistance. As shown in Fig. 12(a), the change of fracture from intergranular dominant mode to transgranular dominant mode is observed as T_{max}^{GB}/T_{max}^G increases. Specifically, the crack primarily grows along the grain boundaries when $T_{max}^{GB}/T_{max}^G < 0.5$. Crack surfaces are created with relatively low level of plastic dissipation as indicated in Fig. 13. When $0.5 < T_{max}^{GB}/T_{max}^G < 1$, both transgranular and intergranular fracture are observed. Although grain boundaries still serve as the damage initiation sites, microcracks which are initiated along the grain boundaries tend to propagate into the neighboring grains, leading to more significant plastic deformation. As shown in Fig. 12 (b), $T_{max}^{GB}/T_{max}^G \approx 1$ corresponds to the transition from intergranular dominated mode to transgranular dominated mode. This indicate that the corresponding T_{max}^{GB} is around 425 MPa, which is exactly the prescribed T_{max}^G. $T_{max}^{GB}/T_{max}^G > 1$ directs the crack to go through grains with a straighter crack trajectory. It is noted in Fig. 12 (b) that the highest J_{IC} value is achieved when L/W reaches its peak. The value of T_{max}^{GB} which corresponds to both peaks is approximately 400 MPa. This trend is in consistence with the result as shown in Fig. 10(b).

It can be concluded that the maximization of both L/W and J_{IC} requires balanced transgranular and intergranular fracture. When intergranular fracture is the predominant failure mode, the damage preferably initiates at the grain boundaries and develops into microcracks. These microcracks quickly coalesce with each other by inducing limited plastic deformation. On the other hand, when transgranular fracture is the only failure mode, the development of microcracks is suppressed. Plastic deformation primarily occurs
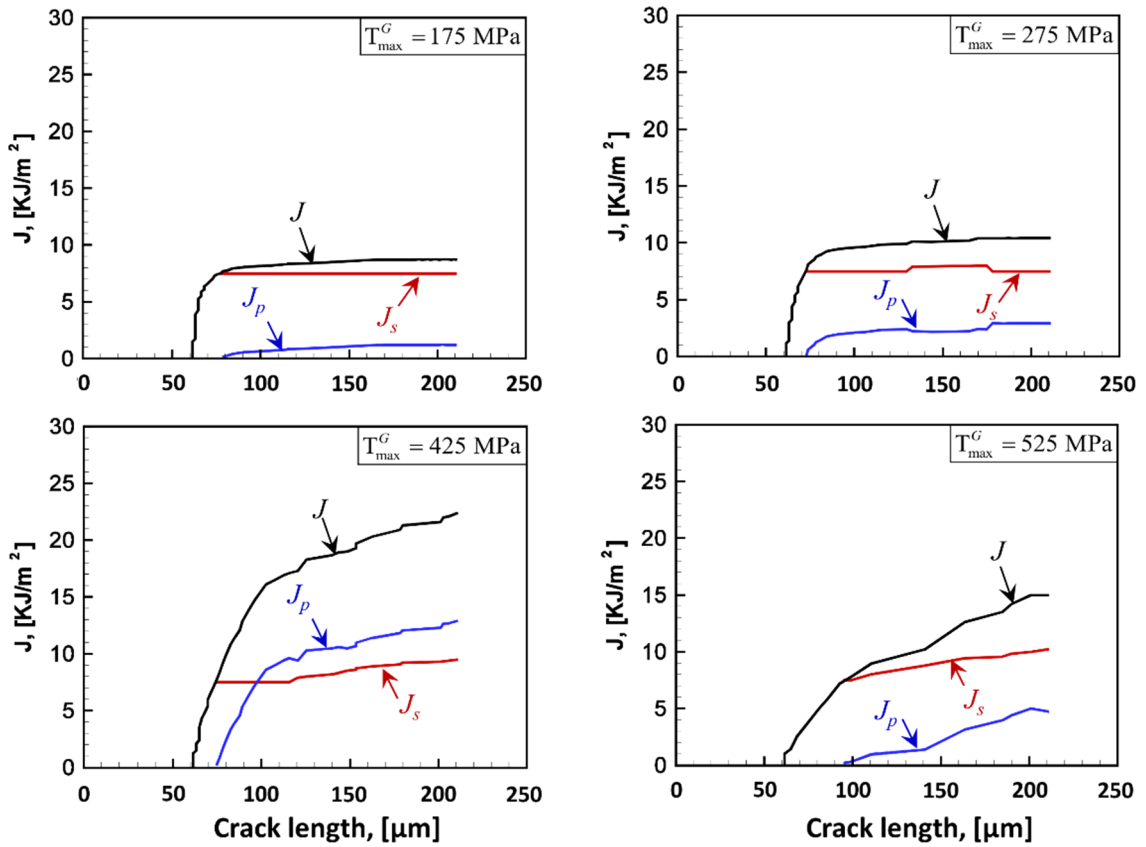
Fig. 11. Contribution of J_s and J_p on the evolution of J under four representative T_{max}^G.

near the pre-crack tip region at the beginning of crack initiation due to crack blunting. Plastic deformation gives way to surface formation as the crack starts to propagate rapidly. When mixed failure mode is activated, microcracks which are initiated from the grain boundaries tend to propagate into the neighboring grains. These uncracked grains allow increased amount of plastic dissipation by serving as "bridges". It is noted that the increase of T_{max}^{GB}/T_{max}^G from 0.6 to 0.95 promotes more microcracks to grow into the grains, leading to increased crack surfaces and plastic dissipation at the same time. This explains why the maximum J_{IC} is reached at $T_{max}^{GB} \approx 400$ MPa with $T_{max}^{GB}/T_{max}^G \approx 0.94$.

4.4. Effect of microstructure morphology

Based on the parametric studies in Sections 4.2 and 4.3, we extend the calculations to multiple microstructures as shown in Fig. 5. The objective is to verify if the above conclusions can be applied to different microstructure instantiations. In this set of calculations, all the grains have the same yield stress with $\sigma_y = 150$ MPa. $\Phi_G = \Phi_{GB} = 7.5$ kJ/m^2 is employed for cohesive elements in the grains and along the grain boundaries. 20 calculations are carried out for each microstructure instantiation by varying T_{max}^{GB}/T_{max}^G from 0.2 to 1.65. It is noticed from Fig. 14 that the predicted J_{IC} values for all the microstructures are almost identical when $T_{max}^{GB}/T_{max}^G > 1.3$. Transgranular fracture is the only failure mechanism as $L_{GB}/W \approx 0$ according to Fig. 15. Grain size has negligible effect on fracture toughness if cracks only go through grains and maintain a straight trajectory since isotropic constitutive relation is assumed for all the grains. It is also noted from Fig. 15 that $T_{max}^{GB}/T_{max}^G \approx 1$ corresponds to the transition point for all microstructure instantiations. This means that the transition from transgranular fracture to intergranular fracture does not depend on the grain size. Grain size influences the J_{IC} prediction when both transgranular fracture and intergranular fracture are activated. As shown in Fig. 14, a microstructure with smaller average grain size has a higher J_{IC} under mixed failure mode. The highest J_{IC} values of microstructure 1 ($\bar{s} = 8.86$ μm) is 23.08 kJ/m^2, which is 15% higher than the highest J_{IC} of microstructure 3 ($\bar{s} = 23.15$ μm). When the grain size is small, the microcracks which initiate along the grain boundaries tend to propagate into the neighboring grains. It can be found in microstructure 1 in Fig. 16 that a significant amount of microcracks propagate into the neighboring grains, leading to more pronounced plastic deformation without compromising the surface energy dissipation. The propagation of cracks from grain boundaries to grains becomes less prominent as the average grain size increases. In microstructure 3, microcracks in grain boundaries quickly coalesce with each other, leading to catastrophic failure of the material. Very few microcracks propagate into neighboring grains as shown in Fig. 16. Therefore, microstructures with small grains tend to have higher fracture toughness since a relatively higher level of plastic defamation can be maintained when most of the cracks still go through the grain boundaries.
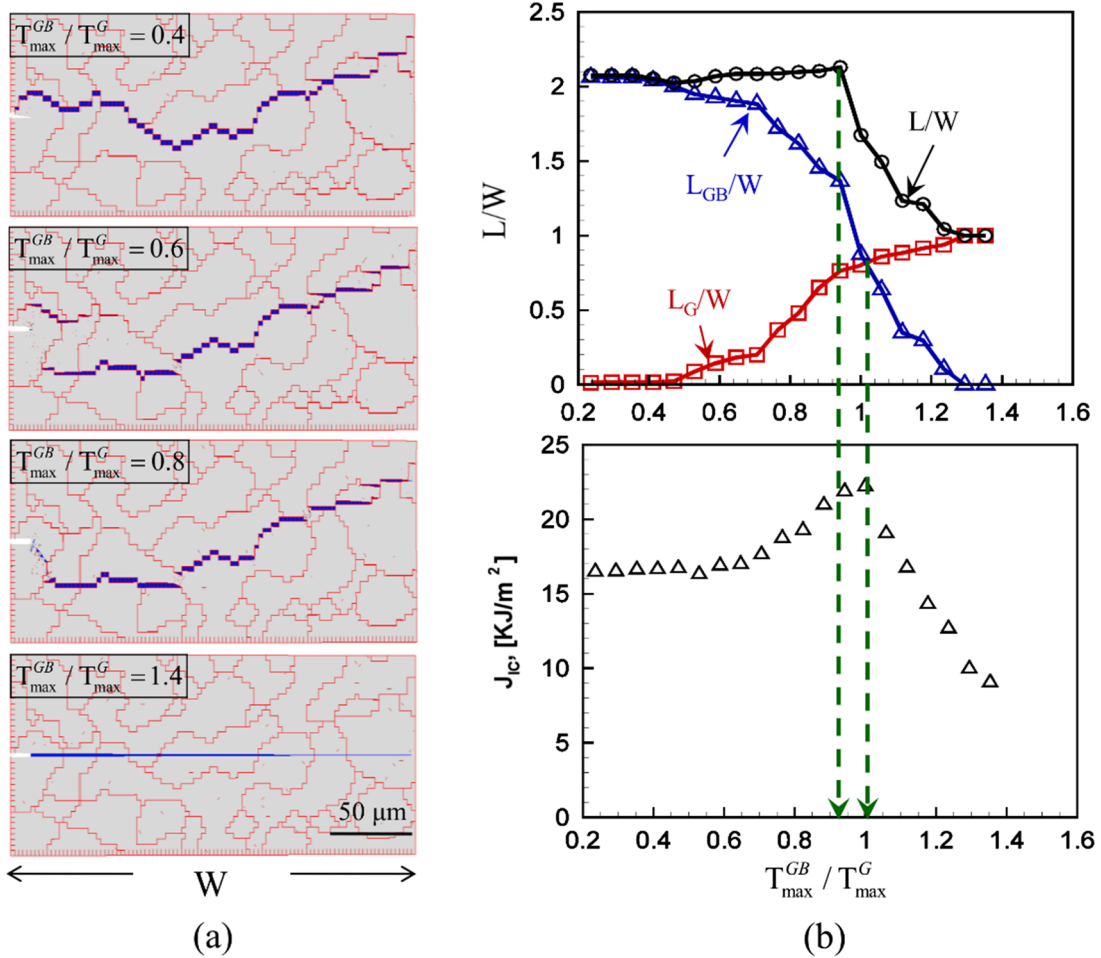
Fig. 12. Illustration of (a) crack trajectory under various T_{max}^{GB}/T_{max}^{G} when $T_{max}^{G} = 415$ MPa and (b) the effect of competing failure mechanisms on fracture toughness.

The simulation predictions can be supported by a few experimental studies on AZ31 Mg alloys. For example, Li. et al [30] experimentally predicted the fracture toughness of AZ31 Mg alloys through the measure of CTOD. They found that the fracture toughness K_{IC} increases from 21.1 MPa$\sqrt{m}$ to 28.6 MPa$\sqrt{m}$ when the grain size decreases from 16.5 μm to 1.8 μm. Somekawa et al. [31] also reported that the fracture toughness of an extruded AZ31 Mg alloy is 22 MPa$\sqrt{m}$ with an average grain size of 13.5 μm. These experimental observations conclude that the grain size refinement can lead to improved fracture toughness of AZ31 Mg, which is consistent with the above simulation predictions. The new physical perspective provided by this computational model is that the grain size refinement induced fracture toughness enhancement is more profound for intergranular fracture dominated failure processes. As shown in Fig. 14, all the predicted J_{IC} values start to saturate at the same plateau when $T_{max}^{GB}/T_{max}^{G} \geqslant 1.4$ regardless of the grain size. This indicates that grain size has negligible effect on fracture toughness improvement when trangranular fracture is the only activated fracture mechanism.

The forgoing analyses point out that the design of polycrystalline metals with improved fracture toughness requires refined grain size and balanced bonding strength in grains and grain boundaries. Pure intergranular fracture or pure transgranular alone cannot lead to maximized fracture toughness. The fundamental avenue for toughening is to create balanced transgranular fracture and intergranular fracture so that the combined energy dissipation in terms of plastic deformation and surface formation can be maximized. Refined grain size can further contribute to the improvement of fracture toughness based on the same T_{max}^{GB}/T_{max}^{G}.

5. Summary

A Cohesive Finite Element Method (CFEM) based multiscale computational framework is developed to evaluate the effects of competing fracture mechanisms in ductile polycrystalline microstructures. This framework allows the competition between material deformation and crack formation as well as the competition between transgranular fracture and intergranular fracture to be quantified by considering the effect of microstructural attributes and constituent behavior. The focus is on relating the microstructure to the macroscopic fracture toughness. The simplified material model tracks the properties of the AZ31 Mg alloy. The fracture toughness
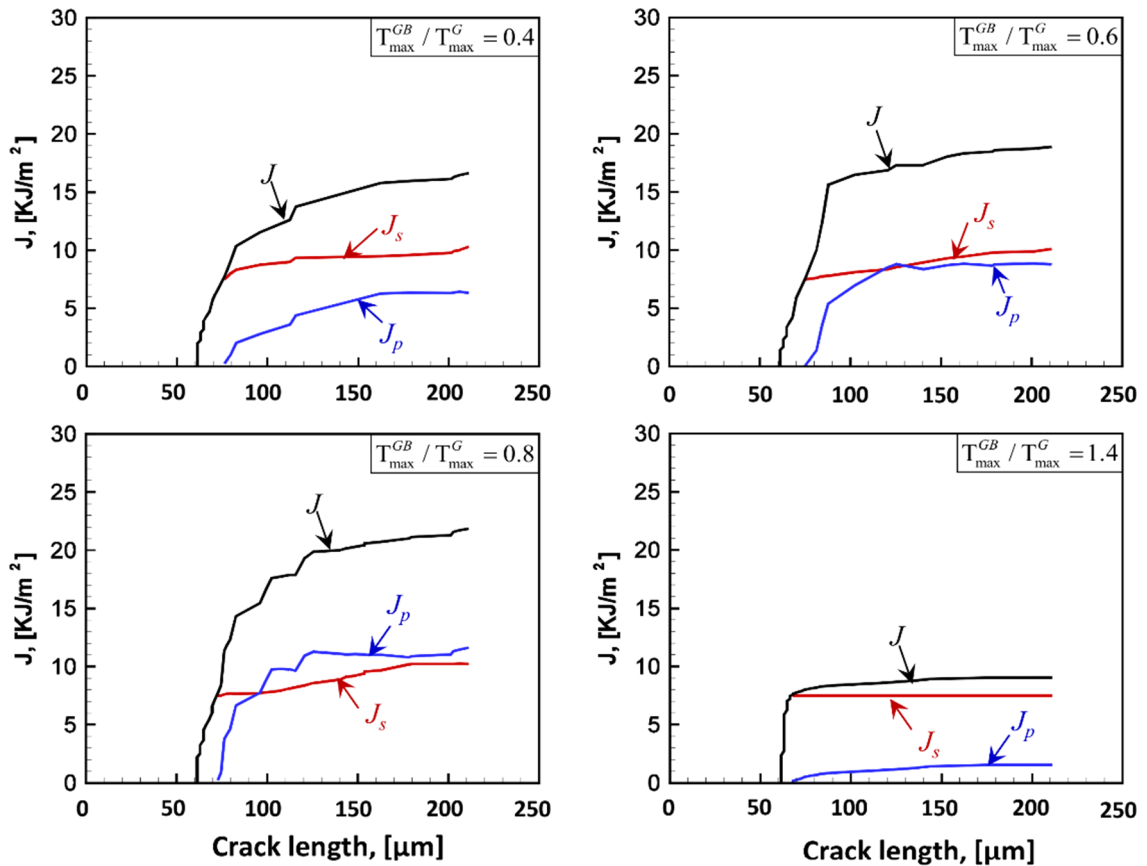
Fig. 13. Contribution of J_s and J_p on the evolution of J under four representative T_{max}^{GB}/T_{max}^{G}.
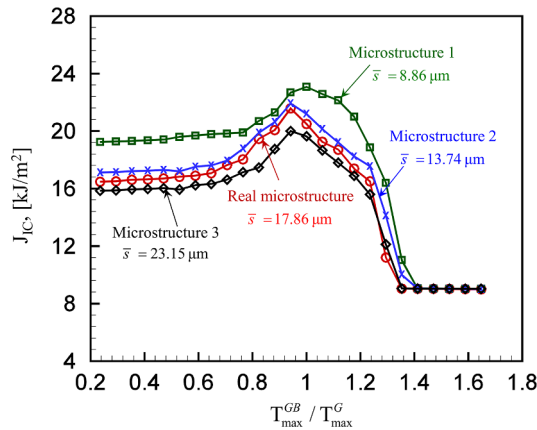

Fig. 14. Effect of grain size on fracture toughness under different T_{max}^{GB}/T_{max}^{G}.

is predicted by calculating the J-integral. The semi-analytical model developed here allows energy dissipation in terms of bulk plastic deformation and crack surface formation to be separately analyzed. Results suggest that the best toughening effect is achieved with balanced transgranular and intergranuar fracture. This requires refined grain size and balanced bonding strength in grains and grain boundaries.

Although the analysis in this study uses material attributes that track the AZ31 Mg alloy, the approach can be applied to other polycrystalline metals as well. The framework developed here provides physical insight in quantifying the competition between material deformation and crack formation as well the competition between transgranular fracture and intergranular fracture. The forging analyses point out that the fundamental avenue for improving the fracture toughness of polycrystalline metals is to promote fracture surface energy release without compromising the plastic energy dissipation. This can be achieved by creating "bridging
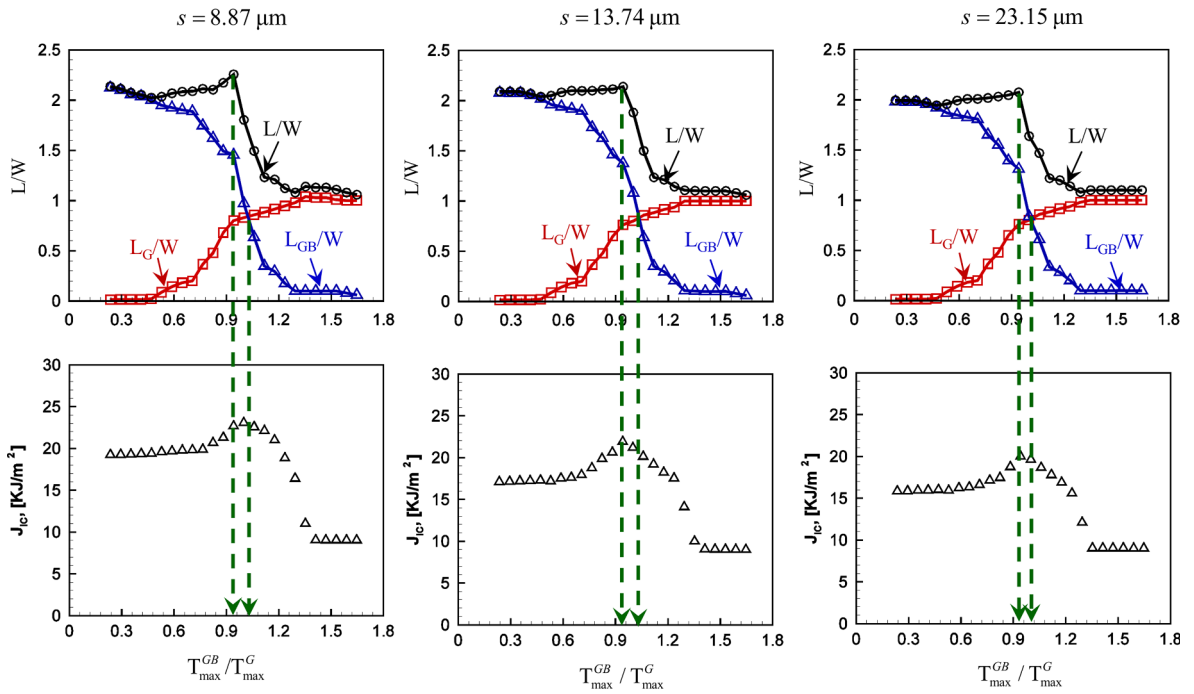
Fig. 15. Competition of transgranuar and intergranular fracture in three microstructures generated by Voronoi tessellation function as shown in Fig. 5.
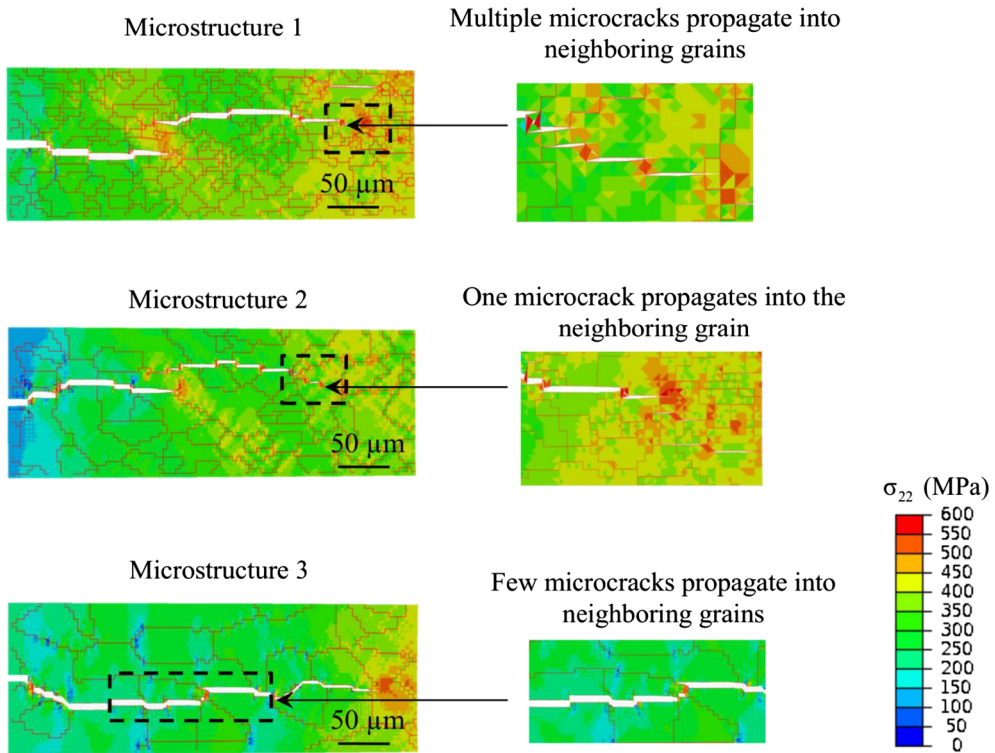

Fig. 16. Illustration of grain boundary microcracks propagate into neighboring grains.

grains" through careful microstructure design. The capability of the current framework can be extended to address grain orientation and texture through implementation of a more advanced constitutive model. As such additional energy dissipation mechanisms taking advantages of bulk constituent anisotropy and grain boundary misorientation effects can be explored, allowing more physical insight and understanding from the energy perspective. This is the topic of a future study.

References

[1] Evans AG. Perspective on the development of high-toughness ceramics. J Am Ceram Soc 1990;73:187–206.
[2] Foulk JW, Johnson GC, Klein PA, Ritchie RO. On the toughening of brittle materials by grain bridging: promoting intergranular fracture through grain angle, strength, and toughness. J Mech Phys Solids Jun 2008;56:2381–400.
[3] Li Y, Zhou M. Prediction of fracture toughness of ceramic composites as function of microstructure: I. Numerical simulations. J Mech Phys Solids Feb 2013;61:472–88.
[4] Li Y, Zhou M. Prediction of fracturess toughness of ceramic composites as function of microstructure: II. analytical model. J Mech Phys Solids 2013;61:489–503. 2//.
[5] Sigl LS. Microcrack toughening in brittle materials containing weak and strong interfaces. Acta Mater 1996;44:3599–609.
[6] Osovski S, Srivastava A, Ponson L, Bouchaud E, Tvergaard V, Ravi-Chandar K, et al. The effect of loading rate on ductile fracture toughness and fracture surface roughness. J Mech Phys Solids 2015;76:20–46. 2015/03/01/.
[7] Srivastava A, Ponson L, Osovski S, Bouchaud E, Tvergaard V, Needleman A. Effect of inclusion density on ductile fracture toughness and roughness. J Mech Phys Solids 2014;63:62–79. 2014/02/01/.
[8] Sgobba S, Geibel B, Blum W. On the constitutive laws of plastic-deformation of inp single-crystals at high-temperatures. Phys. Status Solidi a – Appl. Res. 1993;137:363–79.
[9] Prakash C, Lee H, Alucozai M, Tomar V. An analysis of the influence of grain boundary strength on microstructure dependent fracture in polycrystalline tungsten. Int J Fract 2016;199(1):1–20.
[10] Watanabe T, Tsurekawa S. Toughening of brittle materials by grain boundary engineering. Mater Sci Eng: A 2004;387–389:447–55. 2004/12/15/.
[11] Ludtka GM, Laughlin DE. The influence of microstructure and strength on the fracture mode and toughness of 7xxx series aluminum-alloys. Metall Trans a – Phys Metall Mater Sci 1982;13:411–25.
[12] Simha NK, Fischer FD, Shan GX, Chen CR, Kolednik O. J-integral and crack driving force in elastic–plastic materials. J Mech Phys Solids 2008;56:2876–95.
[13] Zhu X-K, Joyce JA. Review of fracture toughness (G, K, J, CTOD, CTOA) testing and standardization. Eng Fract Mech 2012;85:1–46.
[14] Martinelli A, Venzi S. Tearing modulus, J-integral, CTOA and crack profile shape obtained from the load-displacement curve only. Eng Fract Mech Jan 1996;53:263–77.
[15] Xu XP, Needleman A. Numerical Simulations of Fast Crack-Growth in Brittle Solids. J Mech Phys Solids 1994;42:1397.
[16] Zhai J, Tomar V, Zhou M. Micromechanical simulation of dynamic fracture using the cohesive finite element method. J Eng Mater Technol 2004;126:179–91.
[17] Xu XP, Needleman A. Numerical simulations of dynamic interfacial crack growth allowing for crack growth away from the bond line. Int J Fract 1985;74:253–75.
[18] Needleman A. An analysis of tensile decohesion along an interface. J Mech Phys Solids 1990;38:289–324.
[19] Sun QQ, Guo X, Weng GJ, Chen G, Yang T. Axial-torsional high-cycle fatigue of both coarse-grained and nanostructured metals: a 3D cohesive finite element model with uncertainty characteristics. Eng Fract Mech 2018;195:30–43. 2018/05/15/.
[20] Guo X, Chang K, Chen LQ, Zhou M. Determination of fracture toughness of AZ31 Mg alloy using the cohesive finite element method. Eng Fract Mech 2012;96:401–15. 2012/12/01/.
[21] Chen G, Gao J, Cui Y, Gao H, Guo X, Wu S. Effects of strain rate on the low cycle fatigue behavior of AZ31B magnesium alloy processed by SMAT. J Alloys Compd 2018;735:536–46. 2018/02/25/.
[22] Somekawa H, Mukai T. Fracture toughness in a rolled AZ31 magnesium alloy. J Alloys Compd 2006;417:209–13. 2006/06/29/.
[23] Kobayashi T. Strength and toughness of materials; 2004. p. 50–2.
[24] Sasaki T, Somekawa H, Takara A, Nishikawa Y, Higashi K. Plane-strain fracture toughness on thin AZ31 wrought magnesium alloy sheets. Mater Trans 2003;44:986–90.
[25] Piascik JNR, Dowling N, editors. Fatigue and fracture mechanics, vol. 27. ASTM International; 1997.
[26] Provan GCSAJW. Probabilistic fracture mechanics and reliability. Netherlands: Springer; 1987. p. 97.
[27] Munitz A, Ricker RE, Pitchure DJ, Kimmel G. The influence of thermomechanical treatment on the complex modulus of Mg alloy AZ31. Metall Mater Trans A 2005;36:2403–13.
[28] Barua A, Kim S, Horie Y, Zhou M. Prediction of probabilistic ignition behavior of polymer-bonded explosives from microstructural stochasticity. J Appl Phys 2013;113:184907.
[29] Amstutz GC, Giger H. Stereological methods applied to mineralogy, petrology, mineral deposits and ceramics. J Microsc 1972;95:145–64.
[30] Yu X, Li Y, Li L. Fracture mechanism of AZ31 magnesium alloy processed by equal channel angular pressing comparing three point bending test and tensile test. Eng Fail Anal 2015;58:322–35. 2015/12/01/.
[31] Somekawa H, Mukai T. Effect of texture on fracture toughness in extruded AZ31 magnesium alloy. Scr Mater 2005;53:541–5. 2005/09/01/.